Elastic instability in a family of rectilinear viscoelastic channel flows devoid of centerline symmetry

Shailendra Kumar Yadav [1], Ganesh Subramanian [2,*] and V. Shankar [1,†]
[1]*Department of Chemical Engineering, Indian Institute of Technology, Kanpur 208016, India*
[2]*Engineering Mechanics Unit, Jawaharlal Nehru Centre for Advanced Scientific Research, Bangalore 560064, India*

(Received 12 June 2023; accepted 22 December 2023; published 29 January 2024)

We analyze the linear stability of viscoelastic channel flows, with velocity profiles that are asymmetric about the channel centerline, belonging to the one-parameter Couette-Poiseuille family (CPF). These flows are driven by a combination of an imposed pressure gradient and (tangential) wall motion. A particular member of this family, corresponding to a zero net volumetric flux, may be experimentally realized in a shallow lid-driven cavity flow configuration, as well as in the narrow-gap limit of the Taylor-Couette geometry with an obstruction at a fixed azimuthal angle (a narrow gap Taylor-Dean flow). Recent work by Khalid *et al.* [Phys. Rev. Lett. **127**, 134502 (2021)] has shown, using the Oldroyd-B model, that plane Poiseuille flow with a symmetric velocity profile becomes unstable, even in the absence of inertia, to an elastic "center mode" with phase speed close to the base-state maximum. In contrast, viscoelastic plane Couette flow is linearly stable. The objective of this study is to determine parameter regimes where viscoelastic CPF, whose members include the two limiting flows above, is unstable in the inertialess limit. The dimensionless groups that govern stability are the Weissenberg number $W = \lambda U_{\text{avg}}/L$, the parameter α characterizing the relative importance of Couette ($\alpha = 0$) and Poiseuille flow ($\alpha = 1$) components, and the ratio of solvent to solution viscosities $\beta = \mu_s/\mu$. Here, λ is the polymer relaxation time, L the channel half-width and U_{avg} the average speed; $\beta \in [0, 1]$, and $\alpha \in (-\infty, \infty)$ with $\alpha \to \pm\infty$ representing the unidirectional flow in a shallow lid-driven cavity. We show that, similar to plane Poiseuille flow, an elastic center-mode instability does indeed exist for the aforesaid family in the limit of ultra-dilute polymer solutions ($\beta \gtrsim 0.99$); the instability relies on the existence of a base-state maximum, implying its absence for CPF members with $\alpha \in (-0.5, 0.25)$. Our results point to the potential relevance of the center-mode instability to viscoelastic Taylor-Dean flows and other curvilinear shear flow configurations.

DOI: 10.1103/PhysRevFluids.9.013301

I. INTRODUCTION

The term "purely elastic instability" has traditionally been used to refer to a class of linear instabilities in viscoelastic shearing flows in the absence of inertia. Such instabilities pertain to curvilinear geometries, including the standard rheometric configurations such as the Taylor-Couette, cone-and-plate, and parallel-plate geometries [1–5]. A recent survey of the literature in this regard can be found in reviews by Castillo *et al.* [6] and Datta *et al.* [7]. Purely elastic linear instabilities are driven by hoop stresses present in any curvilinear viscoelastic flow, and must therefore be

*sganesh@jncasr.ac.in
†vshankar@iitk.ac.in

absent in rectilinear shearing flows without a base-flow curvature [8]. Nevertheless, experiments by Arratia and coworkers carried out for pressure-driven flow of highly elastic polymer solutions through a straight channel with a square cross-section, demonstrated the onset of a complex flow state even at very low Reynolds numbers (Re) [9–12], triggered by inlet disturbances in the form of an array of tiny pillars. This transition has been proposed to be governed by a nonlinear subcritical mechanism wherein perturbed streamlines acquire a curvature leading to hoop stresses, that then drive an instability, albeit at a nonlinear order in the perturbation amplitude [9,13,14]. More recent experiments by Steinberg and coworkers have used a rectangular channel with a cross-sectional aspect ratio of about $7:1$, and have again reported instabilities at low Re [15–18]. The experiments involve several variants of a basic channel-flow configuration; while some of the experiments have focused on elastic instabilities localized in the region between a pair of cylindrical obstacles along the channel centerline [15], others have reported coherent structures triggered by an array of pillars at the inlet [16,17], similar to the ones in the experiments quoted above. More recent experiments have uncovered instabilities even in the absence of inlet perturbations [18]. The authors posit [19] linear nonmodal growth, primarily involving spanwise varying perturbations, as the triggering mechanism [20,21].

In contrast to the above scenario, in a recent study, Khalid *et al.* [22] reported a linear instability in viscoelastic plane Poiseuille flow, involving a streamwise varying (that is, 2D) unstable mode, even in the absence of inertia; the elastic stresses in this analysis were modeled using the Oldroyd-B constitutive relation. Although the instability is predicted to occur at high Weissenberg numbers ($W \sim 10^3$), and for ultradilute solutions with solvent-to-solution viscosity ratio $\beta > 0.99$, the discovery of a purely elastic linear instability in a rectilinear shearing flow is nevertheless of intrinsic interest since it points to the existence of an alternate mechanism, unrelated to base-state hoop stresses, that drives the growth of infinitesimal amplitude perturbations. Importantly, subsequent work by Buza *et al.* [23] has used the FENE-P model to demonstrate that accounting for finite extensibility of the underlying polymer molecules causes the said instability to continue down to $W \sim 100$, and $\beta \approx 0.98$, making it more accessible to experimental studies. Furthermore, these authors have shown that the instability is generally subcritical at lower W, becoming supercritical only when $W \geqslant 10^3$, implying that the instability remains accessible to finite-amplitude perturbations even for $W < O(100)$. Another study by Morozov [24] has used direct numerical simulations (DNS) of pressure-driven channel flow, using the linear Phan-Thien-Tanner (PTT) model with the amplitude of the stress nonlinearity tailored to dilute solutions, to demonstrate the existence of nonlinear elastic coherent states in the form of 2D traveling waves in the inertialess limit; these traveling wave structures appear to be the result of a purely elastic self-sustaining process, and for the chosen parameters, lie along the (stable) upper branch of a bifurcation-from-infinity scenario that is assumed to govern the transition to turbulence. On a related note, Lellep *et al.* [25] have recently demonstrated the existence of elastic linear instabilities in shearing flows with profiles approximated by trigonometric functional forms, and with the symmetry of either plane Couette or plane Poiseuille flow, but that satisfy free-slip boundary conditions. The latter conditions lead to the wall mode in the plane Couette analog turning linearly unstable, and both wall and center modes of the plane channel flow analog being unstable, the latter in a larger range of W and β (compared to the predictions of Khalid *et al.* [22]). The authors also showed the unstable modes in the free-slip limit to be a continuation of the least-stable modes in the no-slip limit.

The linearly unstable mode predicted by Khalid *et al.* [22], for viscoelastic channel flow in the absence of inertia, belongs to a class of "center modes" with phase speeds close to the base-flow maximum, and is henceforth termed the "elastic center mode." The unstable center mode has a streamwise velocity disturbance that is symmetric about the channel centerline, and from a fundamental standpoint, it is clearly of interest to examine whether the existence of such a center mode is exclusive to plane Poiseuille flow, with its symmetry correlated to that of the base-state flow itself, or if it is present in more general rectilinear shearing flows devoid of this symmetry. Such asymmetric flows may be modeled using the one-parameter Couette-Poiseuille family, driven by the combination of an imposed pressure gradient and tangential wall motion. A particular member

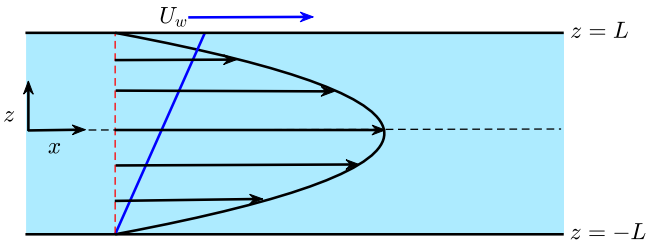

FIG. 1. Schematic of the flow geometry. The base-state flow occurs as a result of the applied pressure gradient and the motion of the top plate with velocity U_w; the bottom plate remains stationary. The velocity profiles shown correspond to the pressure-driven (black) and plate-driven (blue) components.

of this family, corresponding to a zero net volumetric flow rate, may be experimentally realized in a shallow lid-driven cavity configuration. The Couette-Poiseuille family is also of relevance to the so-called Taylor-Dean flow configuration involving a pair of curved walls, with flow driven by both an azimuthal pressure gradient as well as motion of the wall(s) in the azimuthal direction. The said configuration has been realized [26–28] in a Taylor-Couette setup, with the azimuthal pressure gradient arising from a vertical obstruction in the gap at a fixed azimuthal angle; although, the focus of these experiments was on the elastic hoop-stress-driven mode. For gap widths small compared to the cylinder radii of curvature, the Taylor-Dean flow reduces to the lid-driven cavity flow above. Couette-Poiseuille flows are also routinely encountered in lubrication flows between nonparallel surfaces with their separation slowly changing along the flow direction [44]. In such a configuration, a large streamwise pressure gradient arises in the narrow gap to satisfy momentum conservation, while the Couette flow component arises from the relative tangential motion of the two surfaces. Indeed, the pressure generated in the thin gap varies inversely as the gap width, and prevents the two surfaces from coming into contact even in the presence of a large normal load. This feature is exploited, for instance, in the so-called Kugel (or) floating-sphere fountains [45] wherein a very large, heavy, and often rotating, granite sphere is kept afloat by a very thin liquid film maintained via an upward water jet from the bottom.

In the present study, by considering the Couette-Poiseuille family, we address the question of whether centerline symmetry of the base-state velocity profile is an essential ingredient for the elastic center-mode instability. In Sec. II, we discuss the problem formulation and numerical methods used. The salient results are discussed in Sec. III. Section IV summarizes the key conclusions and possible implications of the results obtained in the present study. The Appendix provides a brief summary of the results obtained for the limiting cavity-flow configuration.

II. PROBLEM FORMULATION and NUMERICAL METHOD

A. Governing equations

We consider the pressure-driven flow of an incompressible viscoelastic fluid in a rigid channel of width $2L$, where the top plate moves with velocity U_w while the bottom plate remains stationary, as illustrated in Fig. 1. The viscoelastic fluid is described using the Oldroyd-B model [29], similar to previous studies in this area [22,30–36]. Within the Oldroyd-B framework, the polymer molecule is modeled as an elastic dumbbell with two beads connected by a Hookean spring. Despite limitations such as the inability to capture shear-thinning behavior, the Oldroyd-B model has been shown to provide a reasonable first-cut description of instabilities in both curvilinear [1–3] and rectilinear [6,31–36] shearing flows.

In the governing equations, lengths are scaled by the half-width L, velocities by the average velocity U_{avg}, time by U_{avg}/L, and the pressure and stresses by $\mu U_{\text{avg}}/L$. The average velocity is given by $U_{\text{avg}} = \frac{2}{3}U_{\text{max}} + \frac{1}{2}U_w$, where U_{max} is the maximum of the Poiseuille component and U_w is

the top-plate velocity; note that both $U_{\max}$ and U_w are signed quantities. The total viscosity of the solution is $\mu = \mu_s + \mu_p$, where μ_s and μ_p are the solvent and polymer contributions, respectively. The dimensionless mass and momentum conservation equations, the latter in the creeping-flow limit, are

$$\nabla \cdot \boldsymbol{v} = 0, \tag{1}$$

$$-\nabla p + \beta \nabla^2 \boldsymbol{v} + \nabla \cdot \boldsymbol{\tau} = 0. \tag{2}$$

Here, $\boldsymbol{v} = (v_x, v_y, v_z)$ is the velocity field, p and $\boldsymbol{\tau}$ are the dimensionless pressure and polymer stress fields, respectively, and the parameter $\beta = \mu_s/\mu$ is the ratio of solvent to solution viscosities. The evolution of the polymer stress in Eq. (2) is given by the Oldroyd-B constitutive relation:

$$\boldsymbol{\tau} + W\left(\frac{\partial \boldsymbol{\tau}}{\partial t} + \boldsymbol{v} \cdot \nabla \boldsymbol{\tau} - (\nabla \boldsymbol{v})^T \cdot \boldsymbol{\tau} - \boldsymbol{\tau} \cdot (\nabla \boldsymbol{v})\right) = (1-\beta)(\nabla \boldsymbol{v} + \nabla \boldsymbol{v}^T), \tag{3}$$

where $\beta = 0$ and 1 correspond to the upper-convected Maxwell and Newtonian fluids, respectively. In Eq. (3), $W = \frac{\lambda U_{\text{avg}}}{L}$ is the Weissenberg number, with λ being representative of the longest microstructural (polymer) relaxation time.

The specific base-state velocity profile, to be used in Eqs. (3) and (5), is a member of the Couette-Poiseuille family (CPF), and is given by

$$U_x(z) = (1-\alpha)(1+z) + \tfrac{3}{2}\alpha(1-z^2), \tag{4}$$

where the aforementioned scalings imply that the volumetric flux (per unit span) $\frac{1}{2}\int_{-1}^{1} U_x(z)dz = 1$. For the Oldroyd-B model used here, the above shearing flows are associated with a positive first normal stress difference given by

$$T_{xx} - T_{zz} = 2(1-\beta)W[U'_x(z)]^2, \tag{5}$$

and a zero second normal stress difference.

In Eq. (4), the dimensionless parameter α characterizes the relative importance of plane Couette and plane Poiseuille flow components, being defined as

$$\alpha = 1 - \frac{U_w}{2U_{\text{avg}}}. \tag{6}$$

The various members of the CPF family are obtained for $\alpha \in (-\infty, \infty)$. For $\alpha = 0$ and 1, one recovers the canonical plane Couette and Poiseuille profiles, respectively, along the positive x direction, and the CPF members interpolate between these two flows for $\alpha \in [0, 1]$. Outside of this interval, the plane Couette and plane Poiseuille components are oppositely directed. The plane Couette component is dominant for $\alpha < 0$, with the plane Poiseuille component being dominant for $\alpha > 1$. Both of these CPF sequences asymptote to mirror-image cavity flow profiles, with a net zero volumetric flux, for $\alpha \to -\infty$ and $\alpha \to \infty$, respectively.

The maximum velocity as a function of α is given by $U_{\max} = \frac{(1+2\alpha)^2}{6\alpha}$ and occurs at $z_* = \frac{1-\alpha}{3\alpha}$. This maximum occurs within the physical domain for $\alpha < -0.5$ and $\alpha > 0.25$, moving outside of it for $0 < \alpha < 0.25$ ($z_* > 1$) and $-0.5 < \alpha < 0$ ($z_* < -1$). For α's such that there is an interior maximum [$z_* \in (-1, 1)$], there is a flow reversal within the physical domain at $z_0 = \frac{2+\alpha}{3\alpha}$. In Fig. 2, we show representative velocity profiles for different values of α. The cavity flow above refers to approximately unidirectional flow realized away from the end walls in a shallow lid-driven cavity [44]. In this limit, it is convenient to use the top plate velocity (U_w) as the velocity scale, to yield the velocity profile:

$$U_c(z) = -\tfrac{1}{2}(1+z) + \tfrac{3}{4}(1-z^2). \tag{7}$$

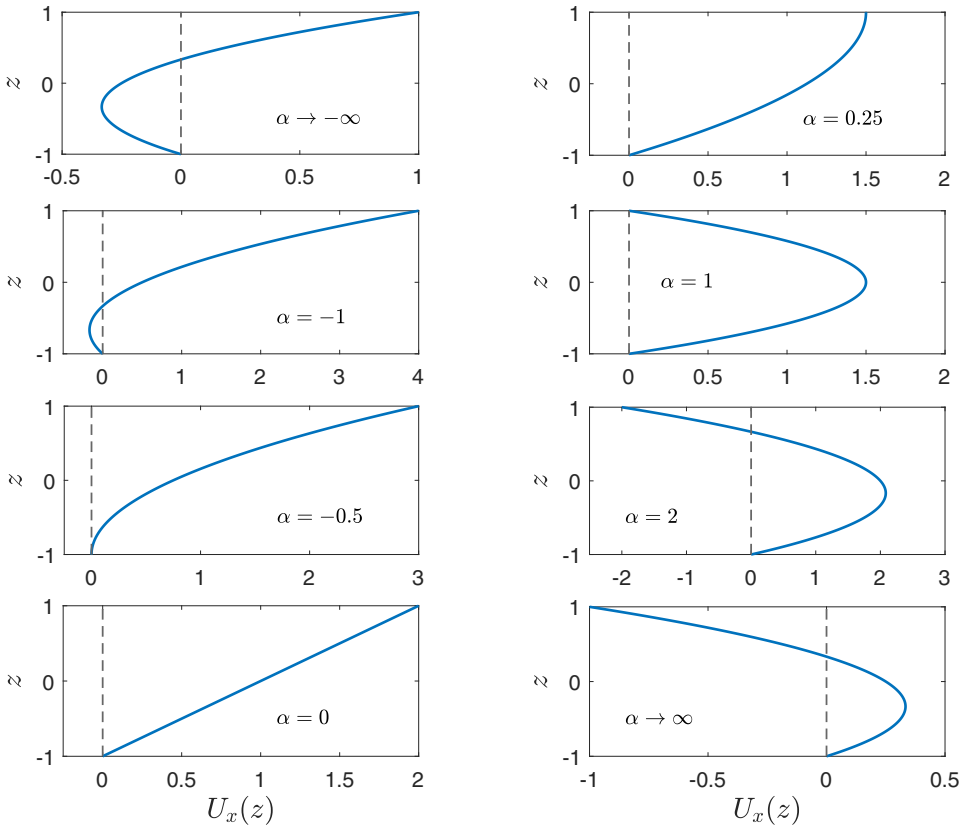

(a) For $\alpha \leq 0$. (b) For $\alpha > 0$.

FIG. 2. The nondimensional base-state velocity profiles for the CPF family for different α: $\alpha = 0$ and 1 represent plane Couette and plane Poiseuille flows, respectively. For $-0.5 \leqslant \alpha < 0.25$, the base flow velocity is monotonic; for $\alpha \to \pm\infty$, the flow reduces to nonmonotonic cavity flows that are mirror images or each other. Note that the cavity flow profile has been nondimensionalized using the top-plate velocity, since the average speed is zero.

The above expression can also be recovered from Eq. (4) as $U_c(z) = \lim_{\alpha\to\infty} \dfrac{U_x(z)}{2\alpha}$. The flow reversal in Eq. (7) occurs at $z = 1/3$, which is the limiting value of z_0 above for $\alpha \to \infty$.

B. Modal stability analysis

We carry out a temporal linear stability analysis of the aforementioned base states in the creeping-flow limit. Within the modal picture, attention is restricted to 2D disturbances since they are more unstable than three-dimensional ones according to Squire's theorem [37]. Thus, we neglect variations in the y direction, and consider infinitesimal amplitude perturbations restricted to the x-z plane, where x is the flow direction and z is the wall-normal direction. All the dynamical variables, e.g., pressure, velocities, and stresses, are perturbed about the laminar base state in Sec. II A above, and are substituted in the nondimensional governing equations, which are further linearized about the base state to furnish a set of linear equations in terms of the perturbed quantities. The

perturbations are expressed in the form of Fourier modes:

$$\hat{f}(x,z;t) = \tilde{f}(z)e^{\{ik(x-ct)\}}, \tag{8}$$

where $\tilde{f}(z)$ is the eigenfunction, k is the (real) wave number in the flow direction, and $c = c_r + ic_i$ is the complex wave speed. The system is unstable (stable) when $c_i > 0$ (< 0). After substituting the ansatz [Eq. (8)] in the linearized versions of Eqs. (1)–(3), we obtain the following set of equations for the perturbation eigenfunctions (with $d_z = d/dz$):

$$ik\tilde{v}_x + d_z\tilde{v}_z = 0, \tag{9}$$

$$ik\tilde{p} - \beta\left(d_z^2 - k^2\right)\tilde{v}_x - ik\tilde{\tau}_{xx} - d_z\tilde{\tau}_{xz} = 0, \tag{10}$$

$$d_z\tilde{p} - \beta\left(d_z^2 - k^2\right)\tilde{v}_z - ik\tilde{\tau}_{xz} - d_z\tilde{\tau}_{zz} = 0, \tag{11}$$

$$\begin{aligned}[1 + ikW(U-c)]\tilde{\tau}_{xx} - 2WU'\tilde{\tau}_{xz} - (1-\beta)[2ik\tilde{v}_x + 4ikW^2U'^2\tilde{v}_x + 2WU'd_z\tilde{v}_x] \\ + (1-\beta)[4WU'U''\tilde{v}_z] = 0,\end{aligned} \tag{12}$$

$$[1 + ikW(U-c)]\tilde{\tau}_{xz} - WU'\tilde{\tau}_{zz} - (1-\beta)[d_z\tilde{v}_x + ik\tilde{v}_z + 2ikW^2U'^2\tilde{v}_z - WU''\tilde{v}_z] = 0, \tag{13}$$

$$[1 + ikW(U-c)]\tilde{\tau}_{zz} - 2(1-\beta)[d_z\tilde{v}_z + ikWU'\tilde{v}_z] = 0. \tag{14}$$

The no-slip and no-penetration boundary conditions at the top and bottom plates are given by

$$\tilde{v}_x(\pm 1) = 0,\ \tilde{v}_z(\pm 1) = 0. \tag{15}$$

We used both spectral and shooting methods to solve the above set of equations. In the spectral method, the dynamical variables are expanded as a finite sum of N Chebyshev polynomials which, when substituted into Eqs. (9)–(15), results in a generalized eigenvalue problem. We used the MATLAB solver "polyeig" for solving this eigenvalue problem. To capture the physically genuine eigenvalues, we ran our code for two different N's, e.g., 450 and 500, and the corresponding eigenvalues are compared with some specified tolerance criterion. We further expand on this aspect at the beginning of Sec. III A. The choice of $N \geqslant 400$ above is to accurately capture the most unstable eigenvalue. The converged eigenvalues from the spectral code were subsequently verified using a numerical shooting procedure [38,39], which involves numerically integrating the linearized governing equations using an adaptive Runge-Kutta method. A Newton-Raphson iterative scheme is then used to determine the eigenvalue, with the initial guess being provided by the spectral method. Since the shooting method does not converge to a spurious eigenvalue, this procedure further ensures that all genuine eigenvalues are obtained from the combination of spectral and shooting methods. Our numerical procedure for computing the spectra for CPF has been benchmarked with the earlier results of Khalid *et al.* [22].

III. RESULTS AND DISCUSSION

Herein, we discuss the results for Couette-Poiseuille flow (CPF) by first describing the eigenspectrum and eigenfunctions, followed by a description of the neutral stability curves. A shorter discussion on the cavity-flow configuration, corresponding to the limit $\alpha \to \pm\infty$, is provided in the Appendix.

TABLE I. Maximum velocity of base flow ($U_{\max}$) and the complex wave speed ($c = c_r + ic_i$) corresponding to the least-stable/unstable center mode for different α; data shown for $k = 0.7$, $W = 800$, and $\beta = 0.994$. For these parameters, the CS is located at $c_i = -0.001785714$.

α	z_*	$U_{\max}$	c_r	c_i
−5	−0.4	−2.7	−2.699729	−0.000431491
−3	−0.4444	−1.3889	−1.388295	−0.00014024
0.6	0.2222	1.3444	1.342496	−0.001173560
0.7	0.1429	1.3714	1.369512	−0.000530702
0.9	0.037	1.4519	1.450578	0.000025312
1.0	0	1.5	1.498996	0.0000424752
1.1	−0.0303	1.5515	1.550702	−0.0000062452
1.3	−0.0769	1.6615	1.660928	−0.0001376691

The center-mode instability [22,33] in viscoelastic plane Poiseuille flow is characterized by an unstable mode with phase speed close to the base-state maximum. For plane Poiseuille flow ($\alpha = 1$), this maximum occurs at the centerline. However, for CPF profiles with $\alpha \neq 1$, the location of the maximum deviates from the centerline (see Fig. 2), and it might then be expected that the phase speed of the center mode should also be a function of the parameter α. The locations of the maxima (z_*), the maximum base flow speeds ($U_{\max}$), and the phase speeds of the least-stable/unstable center mode, given in Table I, show that, even for the asymmetric CPF profiles, the phase speed remains very close to the base-state maximum.

A. Structure of the eigenspectrum and eigenfunctions

In the unfiltered eigenspectra shown in Fig. 3(a)(for two different N's), for $\alpha = 2$, there are several poorly resolved modes that are part of the continuous spectrum (CS) [40–42]. For the Oldroyd-B fluid, there are two continuous spectra, one arising for $\beta = 0$ (the upper-convected Maxwell limit), and the other present only for $\beta \neq 0$. The eigenvalues belonging to these spectra

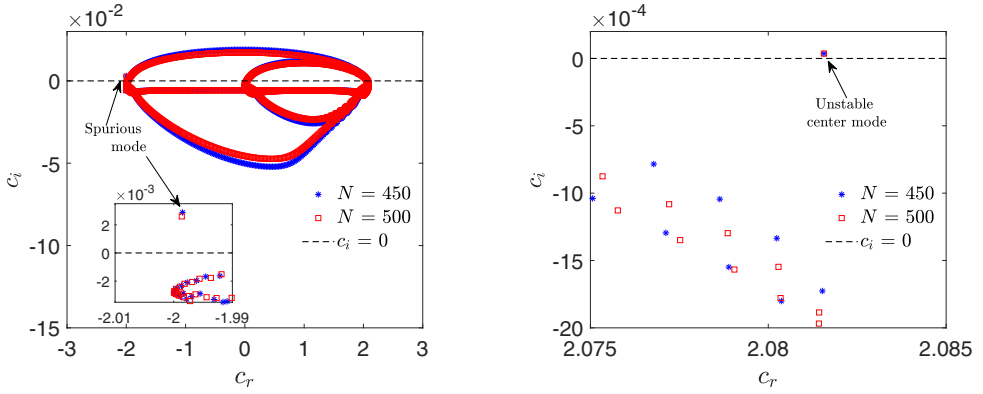

(a) Zoomed-in eigenspectra near $c_i = 0$. (b) Zoomed-in eigenspectra near $c_r = 2$.

FIG. 3. Unfiltered elastic eigenspectra for CPF of an Oldroyd-B fluid with $\alpha = 2$; data shown for $W = 900$, $k = 0.4$, $\beta = 0.995$ and $N = 450$ and 500. The inset in panel (a) shows a poorly converged spurious mode located near $c_r = -2$, which arises in the spectral method (this mode is nonconvergent in the shooting method.) The magnified view in panel (b) shows a (converged) discrete unstable mode with $c = 2.08157 + 0.00003594\,i$.

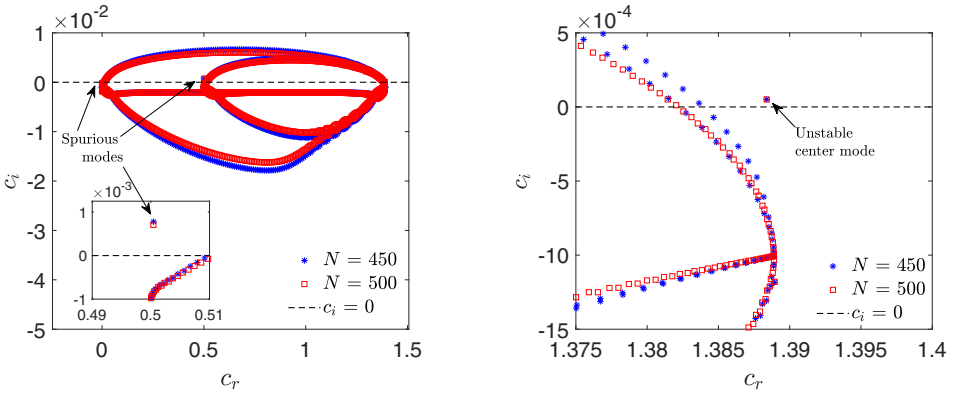

(a) Zoomed-in eigenspectra near $c_i = 0$.

(b) Zoomed-in eigenspectra near $c_r = 1.39$.

FIG. 4. Unfiltered elastic eigenspectra for CPF of an Oldroyd-B fluid with $\alpha = 0.75$; data shown for $W = 2500$, $k = 0.4$, $\beta = 0.995$, and $N = 450$ and 500. Both the main figure and the inset in panel (a) highlight the spurious modes located near $c_r \approx 0$ and 0.5 which remain unconverged in the shooting method. The magnified view in panel (b) shows a (converged) discrete unstable mode with $c = 1.3883837 + 0.00005081\,i$.

have decay rates of $-1/W$ and $-1/(\beta W)$, with phase speeds in the base-state range of velocities, yielding a pair of horizontal lines in the c_r-c_i plane [41]; note that, for $\beta \to 1$, the regime of interest in the present study, these two CS's (horizontal lines) are practically indistinguishable. In any case, the finite numerical resolution in the spectral method implies that these horizontal lines only appear as balloons with a width that is much greater than the theoretical inter-CS spacing. The elastic eigenspectrum shown also contains discrete modes. To isolate the genuine discrete eigenvalues from the spurious ones (belonging, for instance, to the ballooned-up CS), the spectra obtained for two different N's were compared, and only eigenvalues which exhibited convergence to a desired accuracy of six to seven decimal points, were considered genuine. Such converged modes were further corroborated using the shooting method, as already mentioned above. One such discrete mode is the unstable center mode with $c = 2.08157 + 0.00003594i$; the magnified view is shown in Fig. 3(b). The "center mode" terminology has its origins in the Newtonian plane Poiseuille spectrum wherein modes with phase speeds close to the base-state maximum are localized near the channel centerline at sufficiently high Re [39]. The base-state maximum for $\alpha = 2$ is 2.083. The unstable mode in Fig. 3(b) has a phase speed close to this value, and is indeed an analog of the center-mode instability in plane Poiseuille flow ($\alpha = 1$) [22]; we therefore continue to use this nomenclature for $\alpha \neq 1$. While Fig. 3 shows the spectrum for $\alpha > 1$, Fig. 4 shows the spectrum for an α less than unity. The overall features remain analogous to those in Fig. 3, with the unstable mode in particular again having a phase speed close to the base-state maximum.

It has been shown [22] that the streamwise velocity eigenfunction $\tilde{v}_x$ for the unstable center mode in plane Poiseuille flow ($\alpha = 1$) is symmetric about the centerline. For CPF members with $\alpha = 1.5$ and 2, the top plate motion and the flow in its vicinity is in the $-x$ direction, while the bulk of the flow (due to the pressure gradient) is in the $+x$ direction. For purposes of comparison with the symmetric center-mode eigenfunction for the plane Poiseuille configuration, it is thus useful to consider the subdomain $z \in [-1, z_0]$, where the base flow is in the $+x$ direction ($z_0 = 0.7778$ and $2/3$ for $\alpha = 1.5$ and 2, respectively), and additionally, is symmetric about the midpoint ($z_* = -1/9$ and $-1/6$) of this reduced domain. In Fig. 5, we therefore compare the $\tilde{v}_x$ and $\tilde{v}_z$ eigenfunctions for CPF with $\alpha = 1.5$ and 2, the subdomain $z \in [-1, z_0]$ having been rescaled to $z' \in [-1, 1]$ in these figures, to the corresponding eigenfunctions of plane Poiseuille flow—the comparison is for neutral eigenmodes. Table II shows the parameter values used in the comparison shown in Fig. 5 (and in the comparison of the corresponding stress eigenfunctions shown in Fig. 6 below), and

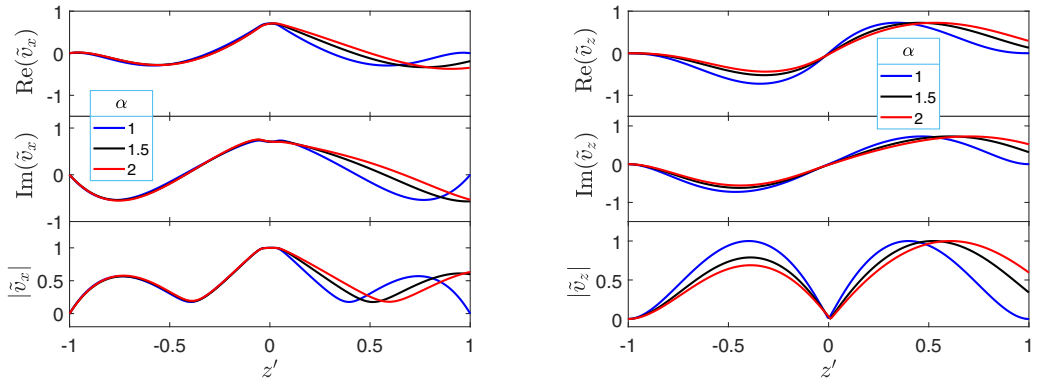

(a) Streamwise velocity eigenfunctions. (b) Wall-normal velocity eigenfunctions.

FIG. 5. Real, imaginary, and absolute values of the (a) streamwise and (b) wall-normal velocity eigenfunctions for CPF of an Oldroyd-B fluid with $\alpha = 1,\ 1.5$, and 2. The data is shown for the neutral eigenmode at $\beta = 0.995$; the other parameter values are given in Table II. For $\alpha = 1.5$ and 2, only the portion of the eigenfunction from $z = -1$ to $z = z_0$ has been plotted, the latter value being the zero-crossing of the base-state velocity profile; further, this domain has been rescaled to $z' \in [-1, 1]$ to facilitate comparison.

TABLE II. The parameters pertaining to velocity and stress eigenfunctions shown in Figs. 5 and 6. The data is shown at fixed value of $\beta = 0.995$.

α	W	k	c_r
1.0	691.27	0.88712	1.4986469
1.5	584.67	0.743	1.7760366
2.0	725	0.49325	2.0814925

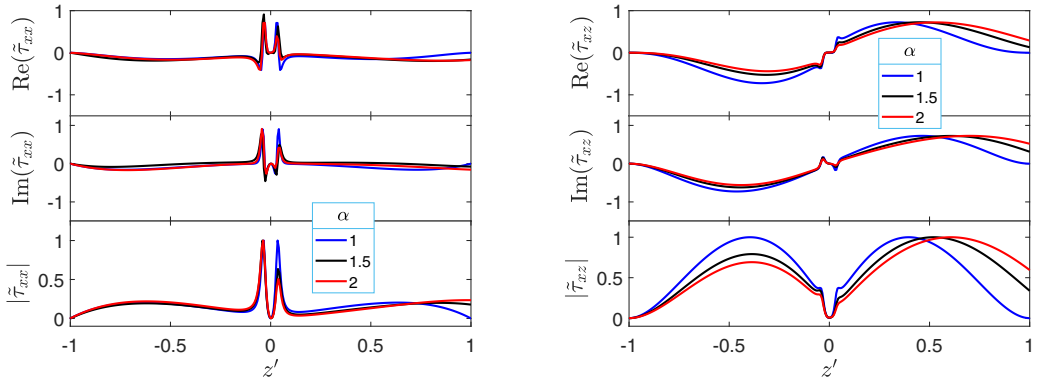

(a) τ_{xx} stress eigenfunctions. (b) τ_{xz} stress eigenfunctions.

FIG. 6. Real, imaginary, and absolute values of the stress eigenfunctions of the (a) streamwise normal stress $\tilde{\tau}_{xx}$ and (b) shear stress $\tilde{\tau}_{xz}$, for CPF of an Oldroyd-B fluid with $\alpha = 1,\ 1.5$, and 2. The data is shown for the neutral eigenmode at $\beta = 0.995$; the other parameter values are given in Table II. For $\alpha = 1.5$ and 2, only the portion of the eigenfunction from $z = -1$ to $z = z_0$ has been plotted, the latter value being the zero-crossing of the base-state velocity profile; further, this domain has been rescaled to $z' \in [-1, 1]$ to facilitate comparison.

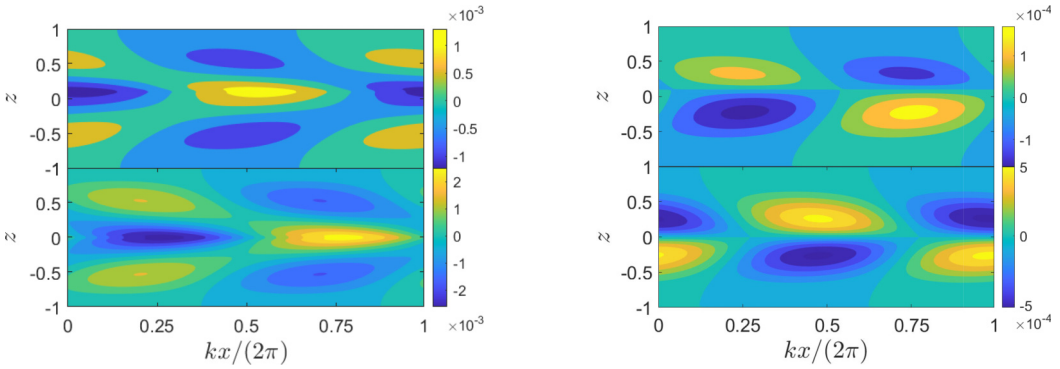

(a) v_x velocity perturbation.

(b) v_z velocity perturbation.

FIG. 7. Contours of the real part of velocity perturbations in $x - z$ plane: (a) the streamwise velocity ($\hat{v}_x$) and (b) wall-normal ($\hat{v}_z$), for CPF of an Oldroyd-B fluid with $\alpha = 2$ (upper subfigure) and $\alpha = 1$ (lower subfigure); data corresponding to parameters shown in Table II.

includes the phase speeds of the neutral eigenmodes. An overall resemblance in the eigenfunction shapes is readily evident. Similar to plane Poiseuille flow, the maximum of the $\tilde{v}_x$ eigenfunction for $\alpha = 2$ occurs near the base-state maximum ($z' = 0$), with the $\tilde{v}_z$ eigenfunction going to zero at the same point. However, the resemblance breaks down near $z' = 1$ for the nonunity α's, since, although the base flow for in these cases is symmetric over $z' \in [-1, 1]$, the eigenfunctions exhibit a weak asymmetry owing to a lack of symmetry in the boundary conditions. Specifically, $\tilde{v}_z$ and $\tilde{v}_x$ do not go to zero at $z' = 1$, unlike the plane Poiseuille case where no-slip conditions are valid at both boundaries ($z = \pm 1$).

The lack of symmetry of the velocity eigenfunctions above, for $\alpha = 1.5$ and 2, carries over to the stress eigenfunctions shown in Fig. 6. The $\tilde{\tau}_{xx}$ eigenfunctions, in particular (for $\alpha \neq 1$), show two sharp peaks of differing amplitudes in the immediate neighborhood, and on either side, of $z' = 0$; this is in contrast to the symmetric twin-peaked structure for plane Poiseuille flow. The structure in the vicinity of these peaks also appear to be a sensitive function of α. The peaks in the perturbation stress profiles for both unity and nonunity α's may be attributed to a pair of "critical layers," on either side of the maximum, where the base flow velocity equals the phase speed of the eigenmode. Since the phase speed is very close to the base-state maximum, the critical layers are in the immediate neighborhood of the latter location. The stress eigenfunctions become singular at these locations for the neutral eigenmode, and exhibit near-singular behavior for small growth rates [6, see footnote on page 5]. Figures 7 and 8 show contour plots corresponding to the velocity ($\hat{v}_x$, $\hat{v}_z$) and polymeric stress ($\hat{\tau}_{xx}$, $\hat{\tau}_{xz}$) perturbations associated with the center mode. A constant x slice of these contour plots is consistent with the eigenfunction plots shown above. In particular, the horizontal streaks in Fig. 8 correspond to the singular peaks of the stress eigenfunctions in Fig. 6.

Khalid *et al.* [22] have shown that the elastic center-mode instability, for plane Poiseuille flow, is present only for $\beta > 0.990552$; although, with the inclusion of inertia, the resulting elastoinertial center mode remains unstable over a wider range of viscosity ratios [33]. For the inertialess case presently under consideration, one might expect a similarly restrictive β interval even for $\alpha \neq 1$. To ascertain this, in Fig. 9, we first examined the CPF profiles with varying α for $\beta = 0.99$, and for $k = 0.1$ [Fig. 9(a)] and 1.0 [Fig. 9(b)]; four different α values, namely 0.25, 0.5, 1, and 2, have been examined. The said figures plot the variation of c_i, the growth rate of the least stable center mode in the CPF eigenspectrum, as a function of W. For the chosen β, we find that c_i remains negative, although it makes a very close approach to neutral stability for $\alpha = 1$ in Fig. 9(a) (see magnified view in the inset). Figure 10(a) explores the effect of α on the least-stable center mode, for $\beta = 0.99$ and $W = 5000$, for different k, and again shows that c_i remains negative. A noteworthy feature in

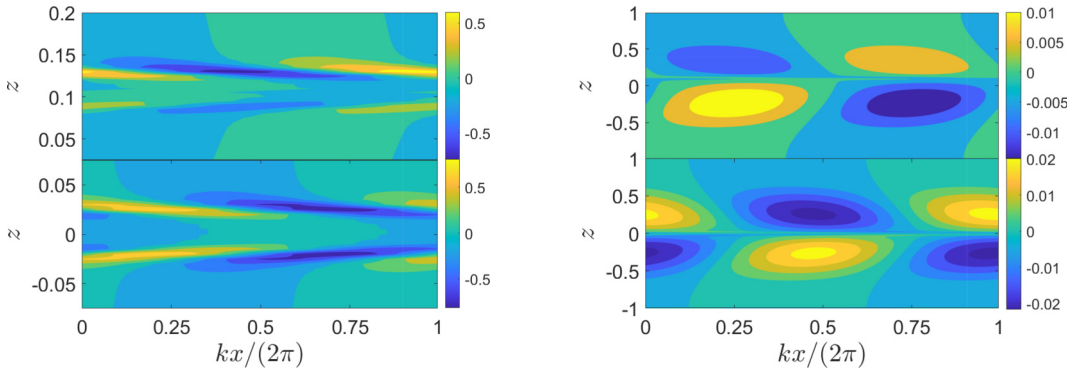

(a) τ_{xx} stress perturbation.

(b) τ_{xz} stress perturbation.

FIG. 8. Contours of the real part of stress perturbations in x–z plane: (a) the streamwise stress ($\hat{\tau}_{xx}$) and (b) shear stress ($\hat{\tau}_{xz}$) for CPF of an Oldroyd-B fluid with $\alpha = 2$ (upper subfigure) and $\alpha = 1$ (lower subfigure); data corresponding to parameters shown in Table II.

this figure is that, for all the k values examined, the center-mode eigenvalue eventually merges with the CS ($kc_i = -1/W$), with decreasing α; see inset of Fig. 10(a). The disappearance of the center mode at a finite α can be understood by noting that for $\alpha = 0$ (plane Couette flow), the spectrum does not have a center mode on account of the monotonic (linear) nature of the velocity profile. As already stated in the context of Fig. 2, the base-flow velocity profile has an interior maximum only for $\alpha > 0.25$, and is monotonic for $0 \leqslant \alpha \leqslant 0.25$. The center-mode instability, in relying on the existence of such a maximum, must necessarily be absent for $\alpha < 0.25$. While $\alpha = 0.25$ does provide a lower bound for instability in this sense, the inset in Fig. 10(a) shows that the center mode merges with the CS even for $\alpha > 0.25$, especially for the lower k's. This feature is also seen in Table I, wherein, as α is decreased to 0.6, the c_i of the center mode gradually approaches that of the CS, and the mode soon disappears into the CS for lower α's, with all other parameters fixed as shown in the table.

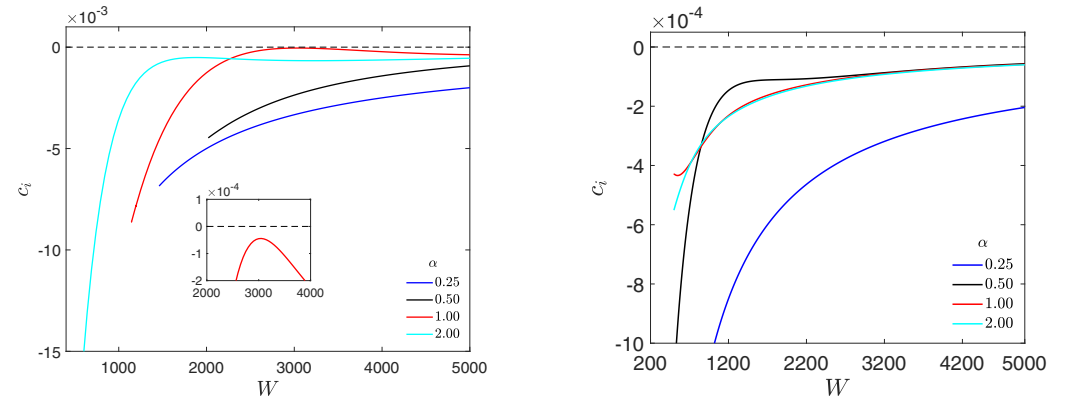

(a) $k = 0.1$.

(b) $k = 1.0$.

FIG. 9. The c_i of the center mode, as a function of W, for different members of the CPF family ($\alpha = 0.25$, 0.5, 1 and 2) and $\beta = 0.99$; (a) $k = 0.1$ and (b) for $k = 1$. The inset in panel (a) shows a magnified view of the region in the vicinity of $c_i = 0$. The flow remains linearly stable in all cases.

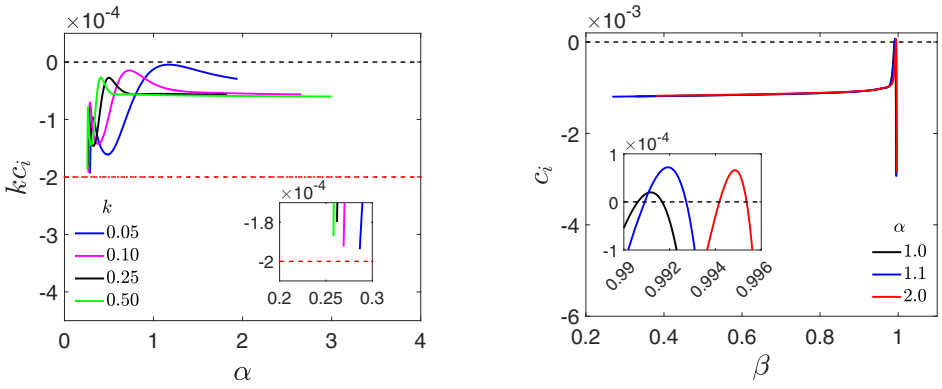

(a) kc_i vs. α. (b) c_i vs. β.

FIG. 10. The variation of c_i for the center mode as a function of (a) α for $\beta = 0.99$, $k = 0.05$, 0.1, 0.25, 0.5; (b) β for different values of α and $k = 0.1$. The inset in panel (a) shows the region near $\alpha = 0.25$, where the center mode merges into the CS. While, the inset in panel (b), shows the narrow range over which the mode is unstable; data for $W = 3200$.

In summary, regardless of α, k and W, CPF remains stable for $\beta = 0.99$. In light of this, Fig. 10(b) shows the variation of c_i with β for members of the CPF family with $\alpha = 1.0$, 1.1, and 2 for a fixed $k = 0.1$. c_i is found to cross zero for a small range of β between 0.991 and 0.993, confirming that, even for $\alpha \neq 1$, the elastic center-mode instability exists over a narrow range of viscosity ratios above $\beta = 0.99$, analogous to the earlier results for plane Poiseuille flow [22].

B. Neutral stability curves

In Fig. 11, we present neutral stability curves demarcating stable and unstable regions in the W-k plane, as a function of α, for different fixed β. For given values of α and β, the flow is unstable within a tongue-shaped region. Analogous to the earlier results of Ref. [22] for plane Poiseuille flow, the instability persists even for $k \ll 1$, and accordingly, the unstable tongue extends to infinity for $k \to 0$, with $W \propto 1/k$ along its upper and lower branches. The unstable tongues exhibit qualitatively different dependencies on α depending on β. For $\beta = 0.994$ in Fig. 11(a), the

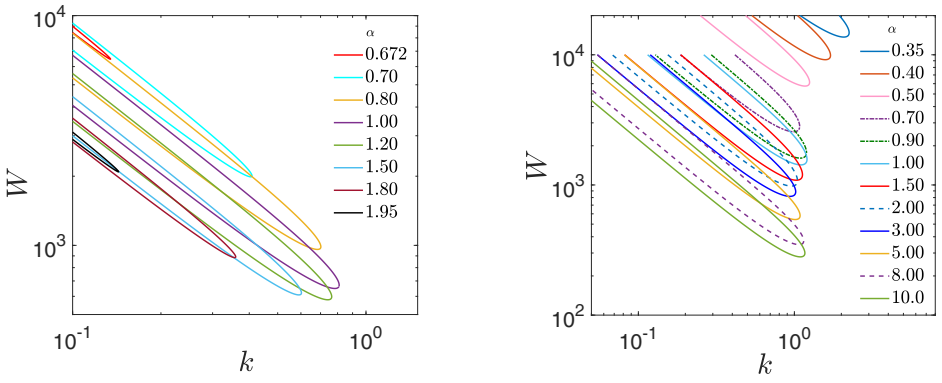

(a) $\beta = 0.994$. (b) $\beta = 0.998$.

FIG. 11. Neutral stability curves in the $W - k$ plane for CPF at various α (>0). (a) Instability is present for $\alpha \in (0.67, 2)$. (b) Instability exists $\forall\, \alpha \gtrsim 0.25$.

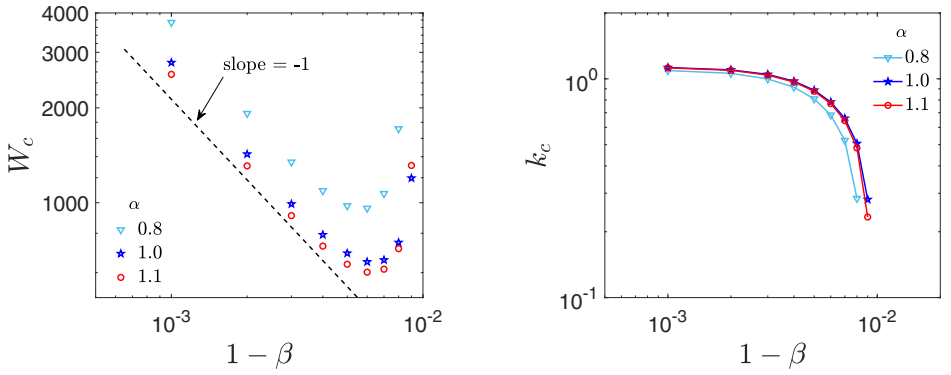

(a) W_c vs. $(1-\beta)$ (b) k_c vs. $(1-\beta)$

FIG. 12. Variation of the (a) critical Weissenberg number (W_c) and (b) the critical wave number (k_c) for $\alpha = 0.8$, 1, and 1.1.

critical Weissenberg number (W_c), corresponding to the minimum W on a given tongue, exhibits a nonmonotonic dependence on α. It attains a minimum ($W_c \approx 580$) for $\alpha \approx 1.2$, and increases in magnitude for α varying on either side of this value. There is a concomitant decrease in the size of the unstable tongue, with the tongue becoming vanishingly small in extent for $\alpha \lesssim 0.67$ and $\alpha \gtrsim 1.95$, implying that CPF is only unstable over a finite interval $\alpha \equiv (0.67, 1.95)$ for $\beta = 0.994$; one finds an analogous behavior for $\beta < 0.994$, with the unstable α interval eventually becoming vanishingly small for $\beta \to 0.99$. For the higher value, $\beta = 0.998$ in Fig. 11(b), W_c decreases monotonically with increasing α. Further, the unstable region remains finite in extent for much smaller $\alpha \approx 0.35$ in Fig. 11(b), receding to infinity for $\alpha \to 0.25^+$. This is consistent with the transition to a monotonic base-flow profile for $\alpha < 0.25$, and with Fig. 10(a) that shows the center mode merging with the CS for $\alpha \to 0.25$. One might naively anticipate the threshold W for CPF to diverge only when $\alpha \to 0$, corresponding to the plane Couette flow limit. However, the above results clearly show that the divergence occurs for $\alpha = 0.25$ or higher, implying that $\alpha > 0.25$ is necessary, although not sufficient, condition for the center-mode instability. In Fig. 11(a), the critical wave number attains a maximum $k_c \approx 0.783$ for $\alpha \approx 1.0$, decreasing to $O(0.1)$ as α approaches the endpoints of the interval of existence mentioned above; in contrast, for $\beta = 0.998$, k_c remains of order unity for any α.

In Fig. 12, the critical parameters W_c and k_c are plotted against $(1-\beta)$ for different α. The variation of W_c in Fig. 12(a) is seen to be nonmonotonic. Since a decrease in β is equivalent to increasing the dissolved polymer concentration, one may interpret this nonmonotonic variation as an increment in polymer concentration initially leading to a decrease in W_c up to $\beta = 0.993$—W_c follows a scaling of $(1-\beta)^{-1}$ for $(1-\beta) \ll 1$; a further increase in polymer concentration leads to an abrupt increase, and eventually, a divergence at a critical β. Similar nonmonotonic behavior and scaling of W_c with $(1-\beta)$ for plane Poiseuille flow is already known [22] and has been included in Fig. 12(a) for comparison purposes. In Fig. 12(b), the critical wave number k_c is seen to decrease gradually with increasing polymer concentration (decreasing β) until $\beta = 0.993$, but decreases very sharply thereafter; again, the k_c variation mimics that known for plane Poiseuille flow (also shown).

Figure 13(a) shows the variation of W_c with α for different β. For $\beta < 0.996$, W_c rapidly increases for both $\alpha \to 0$ and for $\alpha \gtrsim O(1)$. The increase in the former limit is expected since W_c must diverge as $\alpha \to 0.25^+$; it appears that the instability is also absent for $\alpha > 2$ owing to a divergence of W_c. However, for $\beta \geqslant 0.996$, the divergence of W_c at an α of order unity is suppressed, and W_c instead approaches zero as α^{-1} for $\alpha \to \infty$. This change in the large-α behavior is consistent with the different α dependencies of the neutral stability curves already seen in Figs. 11(a) and 11(b). It also

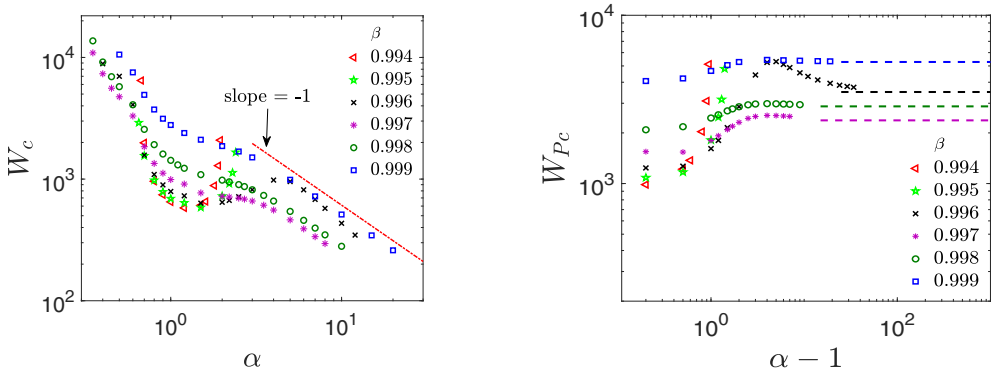

(a) W_c vs. α. (b) W_{Pc} vs. α.

FIG. 13. Variation of the critical Weissenberg numbers (W_c and W_{Pc}) with α ($\alpha > 0$). For $\beta \geqslant 0.996$ and $\alpha \geqslant 2.0$, W_c decreases as α^{-1}, while W_{Pc} asymptotes to a plateau. In panel (b), the dashed straight lines are the large-α asymptotes for cavity flow. The (β, W_{Pc}) pairs from the cavity-flow limit are (0.996, 3499.8), (0.997, 2373.9), (0.998, 2875), and (0.999,5278.4).

leads to a transition, from a nonmonotonic variation of W_c with α for $\beta \leqslant 0.996$, to an eventually monotonically decreasing one for the two highest β's in Fig. 13(a). However, the continued decrease of W_c as α^{-1}, for large α, is an artifact of W being defined based on U_{avg}, and is not to be interpreted as a progressive lowering of the stability threshold. Owing to the U_{avg}-based nondimensionalization, the magnitudes of the top plate velocity and the pressure gradient are adjusted such that the average speed of the nondimensional base-state profile equals unity regardless of α. For large α in particular, the top plate velocity, as well as the pressure-gradient-induced maximum (in the opposing direction), increase as $O(\alpha)$. In this limit, therefore, the relevant velocity scale for defining the Weissenberg number must be the $O(\alpha)$ pressure-gradient-induced maximum, and it is this Weissenberg number that must exceed a finite threshold for instability, implying that W_c must decrease as α^{-1}.

To avoid the aforementioned scaling-induced artifact, we define a new Weissenberg number based on the fact the elastic center-mode instability is driven only by the Poiseuille component of the CPF profile, with c_r being nearly equal to the base-state maximum (see Table I). As a result, the relevant velocity and length scales that dictate the instability ought to be the maximum velocity (U_{maxP}) and the height $L_P = L(z_0 + 1)$ of the Poiseuille component of the flow. Accordingly, the new Weissenberg number is defined as

$$W_P = \frac{\lambda U_{\text{maxP}}}{(L_P/2)}, \tag{16}$$

where $U_{\text{maxP}} = U_{\text{avg}} \frac{(1+2\alpha)^2}{6\alpha}$ denotes the α-dependent maximum velocity mentioned above. W_P and W are related as

$$W_P = \frac{U_{\text{maxP}} W}{(L_P/2)} = W \frac{(1+2\alpha)}{2}, \tag{17}$$

where, in light of the aforementioned physical picture involving a near-cancellation between the wall-driven and pressure-gradient-driven components for large α, the notion of a W_P makes sense only for $\alpha > 1$ (the Poiseuille component, as defined, extends outside the physical domain for $\alpha < 1$). The variation of W_{Pc} (the minimum of the W_P versus k curve) as a function of $(\alpha - 1)$, for different β, is plotted in Fig. 13(b). In contrast to the $O(\alpha^{-1})$-scaling behavior of W_c for $\beta \geqslant 0.996$, W_{Pc} asymptotes to an α-independent plateau for $\alpha \geqslant 2$. In fact, W_{Pc} varies from $\frac{3}{2}W_c$ for $\alpha \to 1$, to $\frac{1}{2}W_\infty$ for $\alpha \to \infty$, where W_∞ is the threshold for the cavity-flow configuration defined using

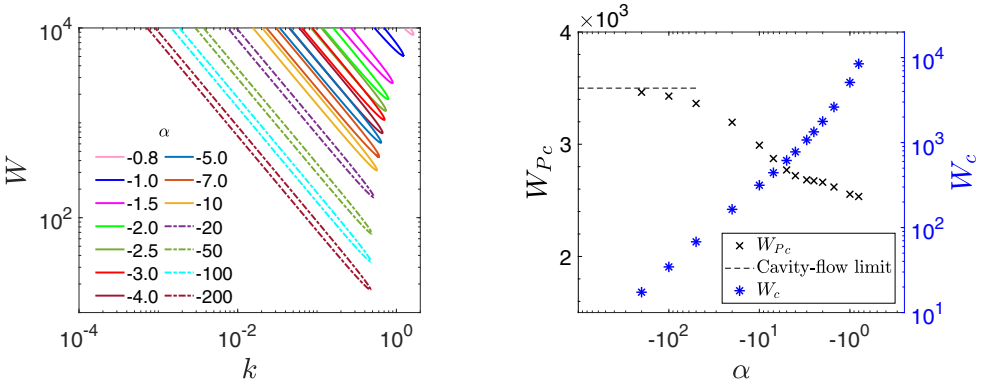

(a) Neutral stability curve.

(b) W_{Pc} vs α.

FIG. 14. Neutral stability curves in the $W - k$ plane and variation of the critical Weissenberg numbers (W_{Pc} and W_c) for $\alpha < 0$. Data is presented at a fixed value of $\beta = 0.996$. (a) Neutral curves shift upwards as $\alpha \to -0.5$. (b) For $\alpha \leqslant -100$, the value of W_{Pc} is nearly equal to the critical Weissenberg number of cavity flow, which is represented as a black dashed line.

the top-plate velocity (see the Appendix); the prefactor $\frac{1}{2}$ stemming from a difference in definitions. The threshold W_∞'s for the cavity-flow configuration appear as dashed horizontal lines in Fig. 13(b), and one observes very good agreement between W_{Pc} (for $\alpha > 50$) and the corresponding cavity-flow thresholds for $\beta \geqslant 0.996$.

Finally, Fig. 14(a) shows the neutral curves for members of the CPF family with $\alpha < 0$. For $\alpha < 0$, the Couette component (in the positive x direction) is dominant over the Poiseuille component (in the negative x direction); the ratio of magnitudes of the maximum velocity of the Poiseuille component to the wall velocity is always lower for CPF members with $\alpha < -0.5$ compared to those for $\alpha > 0.25$. As a result, the width of the neutral tongues in Fig. 14(a) (for $\beta = 0.996$) is significantly narrower compared to the corresponding tongues in the $W - k$ plane for positive α's—this is evident from a comparison of Figs. 11 and 14(a) (despite minor differences in β values). An analogous trend to that in Fig. 13(a) is seen in Fig. 14(b), with W_c again exhibiting a monotonic decrease for $\alpha \to -\infty$. Furthermore, on defining the analog of W_{Pc} above, for negative α's, it is found to converge to the cavity-flow asymptote, albeit at a slower rate, approaching it only for $\alpha < -100$.

IV. CONCLUSION

We have analyzed the modal stability of the Couette-Poiseuille flow (CPF) of an Oldroyd-B fluid in a rigid channel in the creeping-flow regime. Our study shows that the flow becomes linearly unstable via an eigenmode belonging to the class of modes having phase speeds close to the base-state maximum, analogous to the center-mode instability recently found for viscoelastic plane Poiseuille flow [22]. For $\alpha \to \pm\infty$, CPF reduces to the flow occurring in a long rectangular cavity driven by motion of the top plate, and referred to herein as the cavity-flow configuration. Our study predicts the existence of a finite-wavelength ($k \sim 1$) instability, which is affected by both the solvent viscosity ratio β, and the Couette-Poiseuille parameter α. Similar to plane Poiseuille flow, the instability exists only in the ultradilute polymer concentration regime ($\beta > 0.99$). Addition of a Couette component has a stabilizing effect irrespective of the direction of the plate motion, with the CPF profiles for $\alpha < -0.5$ being generally more stable compared to the ones with $\alpha > 1$.

The present study demonstrates that the elastic instability in channel flow is not restricted to the plane Poiseuille profile, but is present in a more general class of rectilinear flows, including the

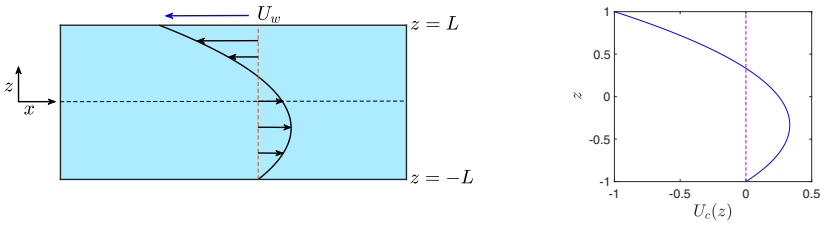

(a) Flow schematics.

(b) Base-state velocity profile for cavity flow.

FIG. 15. (a) Schematic of the flow in a shallow lid-driven cavity; (b) the velocity profile characterizing the unidirectional flow away from the end walls; this profile is a limiting member of the Couette-Poiseuille family, corresponding to $\alpha \to \infty$.

lid-driven shearing flow in a shallow cavity. An instability in the latter configuration is potentially of significance to viscoelastic Taylor-Dean flow in the narrow-gap limit which has been realized in earlier experiments. Although the threshold Weissenberg numbers have been found to be uniformly high in the present effort that uses the Oldroyd-B constitutive relation, we expect the use of the FENE-P model to bring down the thresholds to much lower values [23,43], thus making the present results of relevance to experimental studies. Finally, in so far as the existence of a velocity maximum appears to be a necessary condition for the center-mode instability, it would be worthwhile, in future, to examine if generic base-flow profiles with velocity extrema are capable of supporting a local version of the original center-mode instability. It is also tempting to speculate whether the center-mode instability, identified here for the CPF family, will be of relevance to the viscoelastic analog of Couette-Poiseuille profiles encountered in lubricating flows, similar to the ones seen in Kugel fountains [45].

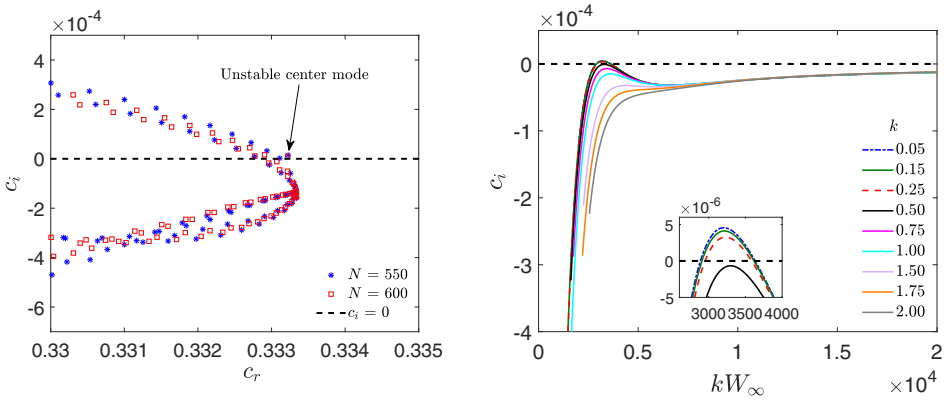

(a) Zoomed-in eigenspectra

(b) c_i vs kW_∞

FIG. 16. Panel (a) shows the zoomed-in unfiltered eigenspectra around $c_r = 0.333$ for cavity flow of an Oldroyd-B fluid with $W_\infty = 7500$, $k = 1$, and $\beta = 0.998$. Spectra are shown at two different collocation points ($N = 550$ and 600) with a discrete eigenvalue, having $c = 0.3332252 + 0.0000148i$. Panel (b) shows the variation of c_i with scaled Weissenberg number (kW_∞) for cavity flow at various wave numbers and fixed $\beta = 0.996$. The inset shows an expanded view of the region where c_i is positive.

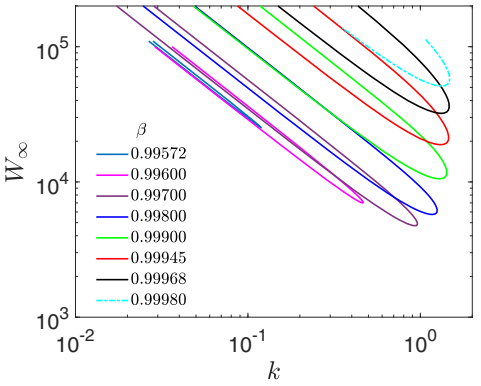

FIG. 17. Neutral stability curves in the $W_\infty - k$ plane, for cavity flow of an Oldroyd-B fluid, for different β.

APPENDIX: THE CAVITY-FLOW LIMIT

Herein, we consider the shallow cavity-flow configuration shown in Fig. 15(a). The flow in such a cavity, at distances from the end walls that are greater than $O(L)$, becomes unidirectional, with the associated velocity profile shown in Fig. 15(b). The appropriate Weissenberg number for this flow is $W_\infty = U_w\lambda/L$, based on the velocity of the moving top plate U_w and the cavity half-height L; the nondimensional profile using these scalings has been defined earlier in Eq. (7). As already mentioned in Sec. I, this unidirectional flow corresponds to the limiting CPF member for $\alpha \to \infty$. For $\alpha \to \pm\infty$, the two cavity flows are mirror images of each other. In these two limits, the base-state velocity profiles and the eigenvalue spectra are also mirror images. However, the neutral stability curves remain same in both $\alpha \to \pm\infty$ limits. In this section, we therefore present the results of cavity flow under the limit as $\alpha \to \infty$.

Figure 16(a) shows a zoomed-in view of the unfiltered eigenspectrum, for the shallow cavity flow of an Oldroyd-B fluid, in the neighborhood of $c_r \approx 0.333$; the spectrum corresponds to $W_\infty = 7500$, $k = 1$, and $\beta = 0.998$. Apart from the continuous spectra, the figure also shows a discrete eigenvalue having phase speed nearly equal to the base-flow maximum ($U_{\max} = 1/3$) and with positive c_i.

Figure 16(b) shows the variation of c_i with the scaled Weissenberg number (kW_∞) for $\beta = 0.996$; c_i is positive over a certain range of W_∞ for $k < 0.5$, but remains negative for $k \gtrsim 0.5$ irrespective of W_∞. Figure 17 shows the neutral stability curves in the W_∞-k plane. The area enclosed by the unstable tongue decreases in extent with decreasing β, becoming vanishingly small for $\beta = 0.99572$. Cavity flow is thus linearly stable for $\beta < 0.99572$. The critical Weissenberg number, $W_{\infty c}$, exhibits a nonmonotonic variation with β, reaching a minimum of $\approx$4750 for $\beta = 0.997$; some of these threshold values appear as horizontal asymptotes in Fig. 13(b).

[1] S. J. Muller, R. G. Larson, and E. S. G. Shaqfeh, A purely elastic transition in Taylor-Couette flow, Rheol Acta **28**, 499 (1989).
[2] R. G. Larson, E. S. G. Shaqfeh, and S. J. Muller, A purely elastic instability in Taylor-Couette flow, J. Fluid Mech. **218**, 573 (1990).
[3] E. S. G. Shaqfeh, S. J. Muller, and R. G. Larson, The effects of gap width and dilute solution properties on the viscoelastic Taylor-Couette instability, J. Fluid Mech. **235**, 285 (1992).
[4] R. G. Larson, Instabilities in viscoelastic flows, Rheol. Acta **31**, 213 (1992).
[5] E. S. G. Shaqfeh, Purely elastic instabilities in viscometric flows, Annu. Rev. Fluid Mech. **28**, 129 (1996).

[6] H. A. Castillo Sánchez, M. R. Jovanovi, S. Kumar, A. Morozov, V. Shankar, G. Subramanian, and H. J. Wilson, Understanding viscoelastic flow instabilities: Oldroyd-B and beyond, J. Non-Newtonian Fluid Mech. **302**, 104742 (2022).
[7] S. S. Datta, A. M. Ardekani, P. E. Arratia, A. N. Beris, I. Bischofberger, G. H. McKinley, J. G. Eggers, J. E. López-Aguilar, S. M. Fielding, A. Frishman, M. D. Graham, J. S. Guasto, S. J. Haward, A. Q. Shen, S. Hormozi, A. Morozov, R. J. Poole, V. Shankar, E. S. G. Shaqfeh, H. Stark *et al.*, Perspectives on viscoelastic flow instabilities and elastic turbulence, Phys. Rev. Fluids **7**, 080701 (2022).
[8] P. Pakdel and G. H. McKinley, Elastic instability and curved streamlines, Phys. Rev. Lett. **77**, 2459 (1996).
[9] V. Bertola, B. Meulenbroek, C. Wagner, C. Storm, A. Morozov, W. van Saarloos, and D. Bonn, Experimental evidence for an intrinsic route to polymer melt fracture phenomena: A nonlinear instability of viscoelastic Poiseuille flow, Phys. Rev. Lett. **90**, 114502 (2003).
[10] L. Pan, A. Morozov, C. Wagner, and P. E. Arratia, Nonlinear elastic instability in channel flows at low Reynolds numbers, Phys. Rev. Lett. **110**, 174502 (2013).
[11] B. Qin and P. E. Arratia, Characterizing elastic turbulence in channel flows at low Reynolds number, Phys. Rev. Fluids **2**, 083302 (2017).
[12] B. Qin, P. F. Salipante, S. D. Hudson, and P. E. Arratia, Flow resistance and structures in viscoelastic channel flows at low re, Phys. Rev. Lett. **123**, 194501 (2019).
[13] A. N. Morozov and W. van Saarloos, Subcritical finite-amplitude solutions for plane Couette flow of viscoelastic fluids, Phys. Rev. Lett. **95**, 024501 (2005).
[14] B. Meulenbroek, C. Storm, V. Bertola, C. Wagner, D. Bonn, and W. van Saarloos, Intrinsic route to melt fracture in polymer extrusion: A weakly nonlinear subcritical instability of viscoelastic Poiseuille flow, Phys. Rev. Lett. **90**, 024502 (2003).
[15] A. Varshney and V. Steinberg, Elastic wake instabilities in a creeping flow between two obstacles, Phys. Rev. Fluids **2**, 051301(R) (2017).
[16] N. K. Jha and V. Steinberg, Universal coherent structures of elastic turbulence in straight channel with viscoelastic fluid flow, arXiv:2009.12258 (2020).
[17] N. K. Jha and V. Steinberg, Elastically driven Kelvin-Helmholtz-like instability in straight channel flow, Proc. Natl. Acad. Sci. **118**, e2105211118 (2021).
[18] Y. Li and V. Steinberg, Elastic instability in a straight channel of viscoelastic flow without prearranged perturbations, Sci. Rep. **13**, 1064 (2023).
[19] V. Steinberg, Elastic turbulence: An experimental view on inertialess random flow, Annu. Rev. Fluid Mech. **53**, 27 (2021).
[20] M. R. Jovanović and S. Kumar, Transient growth without inertia, Phys. Fluids **22**, 023101 (2010).
[21] M. R. Jovanović and S. Kumar, Nonmodal amplification of stochastic disturbances in strongly elastic channel flows, J. Non-Newtonian Fluid Mech. **166**, 755 (2011).
[22] M. Khalid, V. Shankar, and G. Subramanian, Continuous pathway between the elasto-inertial and elastic turbulent states in viscoelastic channel flow, Phys. Rev. Lett. **127**, 134502 (2021).
[23] G. Buza, J. Page, and R. R. Kerswell, Weakly nonlinear analysis of the viscoelastic instability in channel flow for finite and vanishing Reynolds numbers, J. Fluid Mech. **940**, A11 (2022).
[24] A. Morozov, Coherent structures in plane channel flow of dilute polymer solutions with vanishing inertia, Phys. Rev. Lett. **129**, 017801 (2022).
[25] M. Lellep, M. Linkmann, B. Eckhardt, and A. Morozov, Purely elastic linear instabilities in parallel shear flows with free-slip boundary conditions, J. Fluid Mech. **928**, R3 (2021).
[26] Y. L. Joo and E. S. G. Shaqfeh, Viscoelastic Poiseuille flow through a curved channel: A new elastic instability, Phys. Fluids **3**, 2043 (1991).
[27] Y. L. Joo and E. S. G. Shaqfeh, Observations of purely elastic instabilities in the Taylor-Dean flow of a Boger fluid, J. Fluid Mech. **262**, 27 (1994).
[28] Y. L. Joo and E. S. G. Shaqfeh, A purely elastic instability in Dean and Taylor-Dean flow, Phys. Fluids **4**, 524 (1992).
[29] R. G. Larson, *Constitutive Equations for Polymer Melts and Solutions: Butterworth Series in Chemical Engineering* (Butterworth-Heinemann, Oxford, UK, 2013).

[30] M. Zhang, I. Lashgari, T. A. Zaki, and L. Brandt, Linear stability analysis of channel flow of viscoelastic Oldroyd-B and FENE-P fluids, J. Fluid Mech. **737**, 249 (2013).
[31] P. Garg, I. Chaudhary, M. Khalid, V. Shankar, and G. Subramanian, Viscoelastic pipe flow is linearly unstable, Phys. Rev. Lett. **121**, 024502 (2018).
[32] I. Chaudhary, P. Garg, G. Subramanian, and V. Shankar, Linear instability of viscoelastic pipe flow, J. Fluid Mech. **908**, A11 (2021).
[33] M. Khalid, I. Chaudhary, P. Garg, V. Shankar, and G. Subramanian, The centre-mode instability of viscoelastic plane Poiseuille flow, J. Fluid Mech. **915**, A43 (2021).
[34] D. Wan, G. Sun, and M. Zhang, Subcritical and supercritical bifurcations in axisymmetric viscoelastic pipe flows, J. Fluid Mech. **929**, A16 (2021).
[35] D. Wan, M. Dong, and M. Zhang, On the large-Weissenberg-number scaling laws in viscoelastic pipe flows, J. Fluid Mech. **944**, A21 (2022).
[36] M. Dong and M. Zhang, Asymptotic study of linear instability in a viscoelastic pipe flow, J. Fluid Mech. **935**, A28 (2022).
[37] A. Bistagnino, G. Boffetta, A. Celani, A. Mazzino, A. Puliafito, and M. Vergassola, Nonlinear dynamics of the viscoelastic Kolmogorov flow, J. Fluid Mech. **590**, 61 (2007).
[38] T. C. Ho and M. M. Denn, Stability of plane Poiseuille flow of a highly elastic liquid, J. Non-Newtonian Fluid Mech. **3**, 179 (1977).
[39] P. Schmid and D. Henningson, *Stability and Transition in Shear Flows* (Springer, New York, NY, 2001).
[40] M. D. Graham, Effect of axial flow on viscoelastic Taylor-Couette instability, J. Fluid Mech. **360**, 341 (1998).
[41] H. J. Wilson, M. Renardy, and Y. Renardy, Structure of the spectrum in zero Reynolds number shear flow of the UCM and Oldroyd-B liquids, J. Non-Newton. Fluid Mech. **80**, 251 (1999).
[42] I. Chaudhary, P. Garg, V. Shankar, and G. Subramanian, Elasto-inertial wall mode instabilities in viscoelastic plane Poiseuille flow, J. Fluid Mech. **881**, 119 (2019).
[43] G. Buza, M. Beneitez, J. Page, and R. R. Kerswell, Finite-amplitude elastic waves in viscoelastic channel flow from large to zero Reynolds number, J. Fluid Mech. **951**, A3 (2022).
[44] L. G. Leal, *Advanced Transport Phenomena: Fluid Mechanics and Convective Transport Processes* (Cambridge University Press, Cambridge, UK, 2007).
[45] J. H. Snoeijer and K. van der Weele, Physics of the granite sphere fountain, Am. J. Phys. **82**, 1029 (2014).